

## Search for parity nonconserving optical rotation in atomic samarium

D. M. Lucas, R. B. Warrington, D. N. Stacey, and C. D. Thompson  
*Clarendon Laboratory, Parks Road, Oxford OX1 3PU, United Kingdom*

(Received 6 February 1998)

We have searched for parity nonconserving (PNC) optical rotation in five optical transitions within the  $4f^6 6s^2$  ground configuration of atomic samarium using laser polarimetry. It had been suggested that these transitions might be favorable for studying electroweak effects because the upper levels have close-lying levels of opposite parity which might give rise to strong mixing by the PNC Hamiltonian  $H_{\text{PNC}}$ . In terms of the usual parameter  $R [= \text{Im}(\mathcal{E}_{\text{PNC}}/\mathcal{M})]$ , we obtain (in units of  $10^{-8}$ )  $R_{662} = 2.1(1.8)$ ,  $R_{628} = -7(16)$ ,  $R_{611} = -6(8)$ ,  $R_{569} = -17(30)$ , and  $R_{558} = -6(12)$ , where the subscripts give the wavelengths of the transitions. The values of  $R$  are not significantly greater than those already reported for the heavy elements bismuth, lead, and thallium, and we conclude that the samarium transitions do not offer the prospect of a critical test of electroweak theory. Upper limits on the matrix elements of  $H_{\text{PNC}}$  between the upper levels of the transitions and their close-lying opposite-parity neighbors are derived from the results. [S1050-2947(98)06011-9]

PACS number(s): 32.80.Ys, 07.60.Fs

### I. INTRODUCTION

Measurements of parity nonconserving (PNC) effects in atoms provide a test of the standard model of the electro-weak interaction (for recent reviews, see Ref. [1,2]). The experimental accuracy is now at the level of 2% in bismuth [3], 1% in lead [4] and thallium [5], and better than 0.5% in cesium [6], while the best atomic calculations, also for cesium, have an estimated uncertainty of about 1% [7]. The data reported so far are consistent with the standard model, and there is considerable interest in making the comparison more critical [8]. While the experimental accuracy is still far from any fundamental limit, the susceptibility to systematic error makes any significant improvement difficult. The prospect of pushing the atomic calculations much further is likewise daunting; the  $Z^3$  scaling law [9] means that only heavy elements are of practical interest, and for such cases 1% already represents an impressive achievement.

In 1986, it was suggested [10] that PNC effects might be significantly enhanced in the vicinity of certain transitions in the rare earths, so that higher experimental accuracy might be possible. These transitions have the property that one of the levels involved has a neighboring level of opposite parity, so that the two might be strongly mixed by the weak interaction. While there is no immediate prospect of atomic calculations at anywhere near the 1% level in the rare earths, such measurements are still of considerable interest. If one could obtain data in the same transition for different isotopes, the results could be combined in such a way as to provide a test of the standard model which is substantially independent of atomic theory [10]. It has been pointed out [11] that lack of knowledge of the neutron distribution in the nuclei then becomes a problem. However, even comparatively crude measurements would demonstrate immediately and directly that the electron-neutron interaction is the dominant mechanism for producing atomic PNC effects [2]. Further, if results could be obtained for a series of transitions, this would represent the first systematic investigation of PNC effects in a single element, and it might be possible to correlate the results with other atomic properties.

In 1989, spectroscopic studies were reported [12] identifying several allowed magnetic dipole ( $M1$ ) transitions in samarium which might show enhanced PNC effects. Their upper levels  $|\alpha J\rangle$  all belong to the  ${}^5D$  term of the even-parity ground configuration  $\alpha = 4f^6 6s^2$ . The transitions can be observed in absorption; the lower levels (denoted by  $|\alpha J'\rangle$ ) belong to the ground term  $4f^6 6s^2 {}^7F$  (Fig. 1 and Table I), and are thermally populated. The point of interest about the particular levels  $|\alpha J\rangle$  is that they all have close-lying levels of the type  $|\beta J\rangle$ , where the mixture of configurations denoted by  $\beta$  varies from level to level, but has  $4f^6 6s 6p$  as one of its components. The weak interaction can mix this configuration with  $4f^6 6s^2$ , and given the small energy differences between the levels  $|\alpha J\rangle$  and  $|\beta J\rangle$ , there could be strong mixing. Thus if the  $M1$  transitions  $|\alpha J'\rangle$

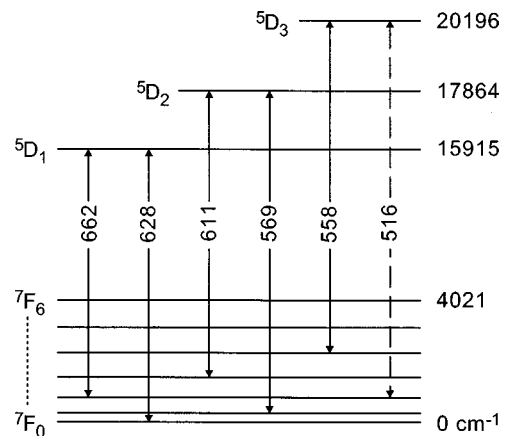


FIG. 1. The energy levels of samarium involved in the  $M1$  transitions studied in the present work. They all belong to the ground configuration  $4f^6 6s^2$ . Vacuum wavelengths of the transitions are given to the nearest nm, level energies to the nearest  $\text{cm}^{-1}$ . Levels and energies are omitted from the  ${}^7F$  ground term for clarity: see Table I and Ref. [12] for further details. The three same- $J$  transitions (e.g.,  ${}^7F_1 \rightarrow {}^5D_1$ ) are not shown since they were too weak to be observed; the 516-nm transition is shown, but was out of the range accessible to our dye laser system.

TABLE I. Properties of the  $M1$  transitions shown in Fig. 1, and of their companion  $E1$  transitions. The  $M1$  transitions are all within the  $4f^6 6s^2$  configuration. The configurational and term assignments for the upper levels of the  $E1$  transitions are from Ref. [17].  $M1$  matrix elements are theoretical [18]; the  $E1$  matrix elements are derived from measurements of transition probabilities [13], and their signs are not known. The energy denominator  $\Delta E = E_{\alpha J} - E_{\beta J}$  as defined in Eq. (3) is the separation of the upper levels of the  $M1$  and  $E1$  transitions.

Wavelength (nm)	$M1$ transition Levels		$M1$ matrix element ( $\mu_B$ )	Wavelength (nm)	$E1$ transition		$\Delta E$ ( $\text{cm}^{-1}$ )
	Upper	Lower			Upper level	$E1$ matrix element ( $ea_0$ )	
662	$^5D_1$	$^7F_2$	-0.467	674	$4f^6 6s 6p$ $^7G_1$	0.020(1)	264
				654	$4f^6 6s 6p$ $^5D_1$	0.432(9)	-198
628		$^7F_0$	0.160	639	$4f^6 6s 6p$ $^7G_1$	0.129(3)	264
				621	$4f^6 6s 6p$ $^5D_1$	0.059(2)	-198
611	$^5D_2$	$^7F_3$	-0.485	603	$4f^5 5d 6s^2$ $^7H_2$	0.274(8)	-211
569		$^7F_1$	0.102	562	$4f^5 5d 6s^2$ $^7H_2$	0.090(2)	-211
558	$^5D_3$	$^7F_4$	-0.454	550	$4f^6 6s 6p$ $^5F_3$	0.081(4)	-264

$-\langle \alpha J \rangle$  are used for PNC studies, one might hope to observe enhanced effects. We describe in this paper an investigation of PNC optical rotation in five transitions of this type. An associated series of measurements of the relative oscillator strengths of  $E1$  transitions of the type  $|\alpha J'\rangle - |\beta J\rangle$  has already been reported [13]; these are important because PNC optical rotation comes about through interference between  $E1$  and  $M1$  amplitudes.

Samarium is much less favorable for optical rotation measurements than bismuth, thallium, or lead, the elements for which high quality data exist; the only previously reported work [14], on two of the present transitions, was able to conclude only that there was no evidence for enhancements significantly greater than a factor of 10 over the typical values in the other elements. The aim of the present work is to assess more critically whether any of the transitions show enhanced PNC effects, in particular to assess the feasibility of a more ambitious investigation of isotopic dependence. In the event, we achieved a precision around an order of magnitude higher than that of Ref. [14], but even at this level it turns out that none of the observed rotations shows any evidence of enhancement, and indeed all are consistent with zero. In the following, we outline the theoretical background, then describe the experiments, and finally discuss the results.

## II. THEORY

### A. PNC optical rotation

According to the standard model, there are terms in the atomic Hamiltonian which cause mixing of states of opposite parity. We are concerned only with the dominant term, which we denote by  $H_{\text{PNC}}$  representing the nuclear-spin-independent interaction between the electrons and the nucleus. We study this mixing by measuring the PNC optical rotation which occurs in an atomic vapor in the vicinity of an  $M1$  transition. The rotation is proportional to the quantity  $R$ , defined in terms of the ratio of the  $E1$  and  $M1$  reduced matrix elements for the transition,  $\mathcal{E}_{\text{PNC}}$  and  $\mathcal{M}$ , respectively:

$$R = \text{Im} \frac{\mathcal{E}_{\text{PNC}}}{\mathcal{M}}, \quad (1)$$

where  $\mathcal{E}_{\text{PNC}}$  comes about because of the very small component of opposite parity mixed by  $H_{\text{PNC}}$  into each of the levels involved in the predominantly  $M1$  transition. Values of  $R$  can be obtained from experiment and compared with theory; it has been shown [15] that the electroweak parameter to which  $R$  is primarily sensitive is the  $Z^0$  mass,  $M_Z$ . Any discrepancy between the value of  $M_Z$  from atomic experiments and the very precise direct measurements at high energy is an unambiguous indication of physics beyond the standard model. Throughout this paper, we give numerical values of  $R$  in units of  $10^{-8}$ .

We now consider the matrix elements in Eq. (1) in more detail. In the case of the  $M1$  absorption lines in samarium, enhanced PNC effects depend on strong mixing in the upper level of the transition. If we neglect lower level mixing, then we may write

$$\begin{aligned} & \langle \alpha JM | \mathbf{d} | \alpha J' M' \rangle \\ &= \sum_{\beta J} \frac{\langle \alpha JM | H_{\text{PNC}} | \beta JM \rangle \langle \beta JM | \mathbf{d} | \alpha J' M' \rangle}{E_{\alpha J} - E_{\beta J}}, \end{aligned} \quad (2)$$

where  $\mathbf{d}$  is the electric dipole operator. Note that  $H_{\text{PNC}}$  connects only states of the same  $J$  and  $M$ , and is independent of the latter.

Normally, there are significant contributions to this sum from several levels, but in the particular case of the transitions considered here the energy denominator is small ( $\sim 200 \text{ cm}^{-1}$ ) for one term (or at most two terms) in the sum. If we assume that this term dominates, as indeed it must if there is to be enhanced rotation due to mixing with the neighboring level, then we have

$$R = \text{Im} \frac{\langle \alpha J | H_{\text{PNC}} | \beta J \rangle \langle \beta J | \mathbf{d} | \alpha J' \rangle}{(E_{\alpha J} - E_{\beta J}) \langle \alpha J | \boldsymbol{\mu} | \alpha J' \rangle}, \quad (3)$$

where  $\boldsymbol{\mu}$  is the magnetic dipole operator and  $|\beta J\rangle$  now refers specifically to the close-lying level. Equation (3) is the basis of our analysis; since the transition operators are vector op-

erators, and Eq. (3) involves only the ratio of their matrix elements, it is convenient to express the latter in reduced form.

The value of  $R$  to be expected in a given transition thus depends on the four quantities in Eq. (3): electric and magnetic dipole matrix elements, an energy denominator, and the PNC matrix element. Unfortunately, no estimates exist for the PNC matrix elements of interest. The levels  $|\beta J\rangle$  consist of admixed configurations [16,17], of which a component is  $4f^6 6s 6p$  (which  $H_{\text{PNC}}$  can connect to  $4f^6 6s^2$ ), but the coefficients are not accurately known. The coupling scheme is also not well enough characterized to give useful information. Values of the other quantities are given in Table I. At the outset of our work, most of the relevant  $E1$  matrix elements were not known; we therefore measured the relative oscillator strengths of the various ‘‘companion’’ lines and put them on an absolute scale using a known upper level lifetime. The  $M1$  matrix elements are theoretical [18], but our work suggests they are sufficiently reliable for the present purposes (see Sec. IV B).

Comparing the situation in samarium with that in the heavy elements bismuth, lead, and thallium, the potential gain of more than two orders of magnitude in the energy denominator is partially offset by the comparatively low  $E1$  matrix elements. Nevertheless, if we simply assume in the absence of other evidence that the PNC matrix elements in samarium are typically smaller than the dominant contributions in these heavy elements by a factor of order 2 due to the  $Z^3$  factor, we find that there is still the prospect of enhancement by around an order of magnitude. The fact that this is not observed in practice implies that the PNC matrix elements are substantially smaller than simple scaling suggests (see Sec. VI).

The  $M1$  matrix elements in Table I vary considerably, and it might appear from Eq. (3) that a low value would be advantageous. However, this is not the case [19]; the rotation one actually measures for a given column length and vapor pressure is proportional to the quantity

$$R|\mathcal{M}|^2 = \text{Im}(\mathcal{E}_{\text{PNC}} \times \mathcal{M}). \quad (4)$$

The reason this is important is that a practical limit on the optical depth (of a given transition) at which one can work is set by the significant background absorption in samarium (see Sec. IV). Hence, although for a given  $E1$  admixture and absorption length, weaker  $M1$  lines have larger rotations, one cannot take advantage of this in samarium because of the attenuation of the light.

Finally, it is of interest to consider the ratio  $R_1/R_2$  for two transitions from the same upper level to the lower levels  $|\alpha J'_1\rangle$  and  $|\alpha J'_2\rangle$ :

$$\frac{R_1}{R_2} = \frac{\langle \alpha J | \boldsymbol{\mu} | \alpha J'_2 \rangle}{\langle \alpha J | \boldsymbol{\mu} | \alpha J'_1 \rangle} \times \frac{\langle \beta J | \mathbf{d} | \alpha J'_1 \rangle}{\langle \beta J | \mathbf{d} | \alpha J'_2 \rangle}. \quad (5)$$

Thus the unknown parity admixture of the upper level cancels, leaving a simple expression for the ratio of electroweak effects in terms of the known strengths of allowed  $M1$  and  $E1$  transitions. The expression is only valid if the PNC rotation is mainly due to admixture with the neighboring level, but it is useful even if this is not the case. For example, if a

measurement of  $R$  in the transition  $|\alpha J'_1\rangle - |\alpha J\rangle$  shows no enhancement, then one will not expect any in  $|\alpha J'_2\rangle - |\alpha J\rangle$  either.

## B. Rotation and absorption spectra

An experimental value for  $R$  is obtained as follows. The optical rotation as a function of frequency in the vicinity of the transition is given by

$$\phi_{\text{PNC}}(\nu) = pRD(\nu), \quad (6)$$

where

$$p = \frac{\pi\mu_0}{3\lambda\hbar} \frac{|\mathcal{M}|^2}{(2J'+1)} \int N(z) dz. \quad (7)$$

Here  $\lambda$  is the wavelength of the transition, and the line integral gives the atomic number density  $N(z)$  in the lower level integrated along the path  $z$  of the beam. The line-shape function  $D(\nu)$  is the convolution of a dispersion curve with a Gaussian function, representing Doppler broadening (explicit expressions for this and the other line-shape functions used in our analysis are given in Ref. [20]). Formulas (6) and (7) are appropriate to a single isotope with nuclear spin  $I=0$ , or with negligible hyperfine structure in the transition of interest. When there are several isotopes present, as in the case of samarium, the rotation is simply the sum of those occurring for each individually. In fact, in the transitions of interest here the hyperfine structure is very small, and unresolved in our experiments, and likewise the isotope shift. We therefore make simple approximations in the fitting procedure, as explained below in the discussion of the data analysis, and Eqs. (6) and (7) are sufficient for our purposes.

The quantity  $p$  is determined from the absorption spectrum. The transmission  $\alpha(\nu)$  of the atomic vapor as a function of frequency  $\nu$  is given by

$$\alpha(\nu) = \exp[-b(\nu) - pV(\nu)], \quad (8)$$

where the line-shape function  $V(\nu)$  is a Voigt profile, the convolution of Lorentzian and Gaussian functions, normalized such that  $\int V(\nu) d\nu = 1$ . Thus  $pV(\nu)$  represents absorption due to the  $M1$  transition. However, there is also background absorption represented by  $b(\nu)$  which must be allowed for (see Sec. V E 1). We neglect any electric quadrupole contribution to the line strength; calculations [18] suggest that this amounts to no more than a few percent in any of the transitions studied here.

It is necessary to introduce a further rotation spectrum, that due to a longitudinal magnetic field (the Faraday effect). It is not practicable to screen out magnetic fields to the level at which their effects can be neglected, so the experimental rotation spectra contain a Faraday contribution. For a single even isotope, as before, and considering only the case in which the Zeeman splitting of the levels involved is much less than the linewidth (a condition well fulfilled in our experiments), we obtain

$$\phi_F(\nu) = \chi \frac{\partial}{\partial \nu} D(\nu), \quad (9)$$

where

$$\chi = \frac{\mu_0 \mu_B}{4\lambda \hbar^2} \frac{|\mathcal{M}|^2}{(2J'+1)} \int B(z) N(z) dz \times \sum_{M', M} \begin{pmatrix} J & 1 & J' \\ -M & 1 & M' \end{pmatrix}^2 \langle g + M'(g - g') \rangle. \quad (10)$$

The sum is over the magnetic quantum numbers  $M$  and  $M'$  of the upper and lower levels, respectively, which have magnetic  $g$  factors  $g$  and  $g'$ , and the integral over the optical path now contains the magnetic field  $B(z)$ .

In our experiments, since we are interested only in allowing for Faraday rotation in our spectra,  $\chi$  is not required explicitly; it does not affect the line shape, giving simply a scaling factor. This is fortunate since the  $g$  factors of the upper levels of the transitions of interest are not known, and neither is the precise form of the magnetic-field distribution. However, the assumption that the result for a single even isotope is sufficiently accurate is much more open to question than is the case for the spectra of PNC rotation and absorption; any misrepresentation of the Faraday profile in our analysis could give an apparent PNC contribution. In particular, the Faraday and PNC rotation spectra are orthogonal functions for a single even isotope, being even and odd, respectively, about line center, whereas the presence of an isotope shift and hyperfine structure can cause an antisymmetrical PNC-like component in the former. We therefore investigated the Faraday rotation for all the lines studied at fields high enough for PNC effects to be quite negligible [but still well within the range of validity of Eq. (9)], and in most cases used these empirically determined profiles in our fits to allow for magnetic rotation in our PNC data. This is discussed further below in Sec. V, together with other features of the analysis procedure.

### III. SAMARIUM TRANSITIONS

There are nine allowed  $M1$  transitions from the  $4f^6 6s^2 \ ^7F$  term to the  $4f^6 6s^2 \ ^5D_{1,2,3}$  levels, of which we studied five (see Fig. 1). We excluded the three transitions between levels of the same  $J$  because they are very weak (see Table I). This is because the breakdown of  $LS$  coupling leads to an admixture of  $^7F$  into  $^5D$ , and vice versa, and both these terms have the same  $g$  factor. To the approximation that no other term contributes to the admixture, the transition probability vanishes. The authors of Ref. [12] searched for the transition at 640 nm ( $^7F_1 - ^5D_1$ ), but were unable to observe it. Neither of the other two, 586 nm ( $^7F_2 - ^5D_2$ ) and 535 nm ( $^7F_3 - ^5D_3$ ), was strong enough to appear under our experimental conditions. Finally, the 516-nm transition ( $^7F_2 - ^5D_3$ ) was out of the range accessible with our dye laser system.

### IV. EXPERIMENT

#### A. Polarimeter

The measurements were carried out using the laser polarimeter which had been developed for earlier experiments on bismuth transitions [3,21]. It permits the rotation and absorption spectra produced by an atomic vapor to be recorded over

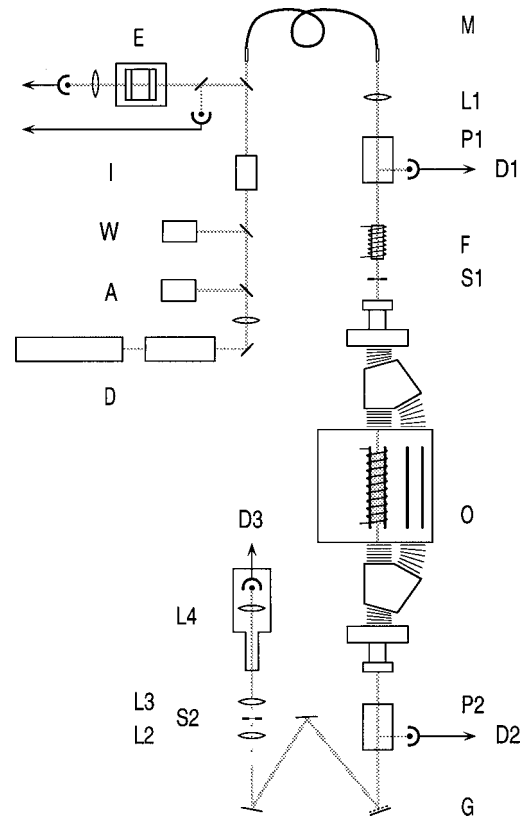


FIG. 2. The experimental system. For key, see text. For details of the oven, see Fig. 3.

a range of up to 30 GHz at any wavelength accessible to our tunable dye laser. It is shown schematically in Fig. 2. There were minor variations in the system during the two-year period the measurements were carried out (e.g., for different spectral lines), but for the great majority of the work it was as described in the following. The laser system  $D$  (Coherent Innova 200 argon ion pump, and Coherent CR699 dye laser) is on a floating optical table together with diagnostic equipment (spectrum analyzer  $A$  and wavemeter  $W$ ) and a scan calibration system. The latter consists of a plane Fabry-Perot etalon  $E$  of 80.026-mm spacing, which forms a fringe pattern in the focal plane of a lens; the intensity at the center of the pattern is monitored and normalized using the output of a separate detector, giving fringes 1.8726 GHz apart. The main laser beam is matched into a polarization-preserving mono-mode fiber  $M$  which transfers the light to the specially constructed floating polarimeter table. This is 6 m long by 0.6 m wide, and was designed so as to keep flexing and vibration to a minimum. The beam power at the fiber output varied from one wavelength to another, but was typically 100 mW. The essentials of the optical system are the crossed polarizers  $P1$  and  $P2$  in between which are a Faraday modulator  $F$  and the samarium oven  $O$ , and a detector  $D3$ , a low-noise photodiode type SDO41, supplied by Silicon Detector Corporation (SDC), to monitor the transmitted intensity.  $P1$  and  $P2$  were designed to avoid contamination of the transmitted beam with light present due to reflections at the polarizer surfaces, a common problem with commercial devices; each consists of two  $30^\circ$  calcite prisms in series, the second inverted with respect to the first. An incident beam polarized in the ‘‘transmission’’ direction of  $P1$  or  $P2$  emerges parallel with its

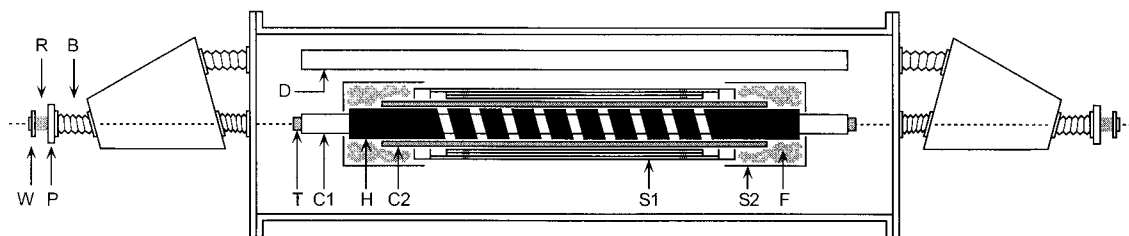


FIG. 3. The oven. For key, see text. The scale is approximately 1:12. Not shown are vacuum ports or leadthroughs, the thermocouple, water-cooling pipes attached to the outside of the chamber and its end plates, the field coil wound around the chamber, and the outer mu-metal shield. The oven is shown in the "samarium" position, where the light path (dotted line) lies through the center of the tube  $T$  containing samarium vapor, rather than in the "dummy" position, where the light would pass through the empty tube  $D$ .

original direction of propagation, having traversed both prisms, while an orthogonally polarized beam is deflected sufficiently by the first prism for it to miss the second. The modulator is the basis of the angle-measuring system (see Sec. IV D). It consists of a solid cylinder of a glass with a high Verdet constant (Hoya FR-5) to which is applied a modulated magnetic field, so as to produce rotations of  $\phi_m$ ,  $-\phi_m$  and 0 in a programmed sequence, where  $\phi_m \sim 10^{-3}$  rad; the exact value is chosen to optimise the signal-to-noise ratio in the angle measurement.

Other components in the optical system are as follows. An optical isolator  $I$  in the output beam from the laser was found necessary for some of the lines because of back reflection from the input tip of the fiber. Two detectors  $D1$  and  $D2$  monitor the laser intensity before and after the oven (see Sec. IV D below).  $D1$  uses a reflection from one of the prisms comprising  $P1$ , while  $D2$  intercepts the strong beam from the analyzer polarized at right angles to the signal beam. Between the analyzer and the main signal detector  $D3$  is a diffraction grating  $G$  to reduce the background due to thermal radiation from the oven. There are also two shutters  $S1$  and  $S2$ .  $S1$ , before the oven, allows the background signals from  $D2$  and  $D3$  to be recorded without laser light, but with the residual oven light; this is necessary for optimum reduction of laser intensity noise by normalization. The purpose of  $S2$  is to prevent saturation of the detector while the oven is being heated. Heating is done electrically, and gives rise to a large Faraday rotation in the samarium vapor which causes light levels at  $D3$  to be high enough to require a prohibitively long detector recovery time unless they are screened off. Finally, there are four converging lenses  $L1$ ,  $L2$ ,  $L3$ , and  $L4$  on the polarimeter table to shape the beam.  $L1$ , of focal length 800 mm, immediately prior to  $P1$ , ensures that the beam diameter does not exceed a few mm while traversing the polarimeter.  $L2$  ensures that the shutter  $S2$  is at a small waist.  $L3$  produces an approximately collimated beam, while  $L4$  focuses the light onto  $D3$ .

### B. Oven

The oven is shown in Fig. 3; it is that used for the work on bismuth [3,21] with some modifications because of the high reactivity of samarium and the higher temperatures required. It consists essentially of a cylindrical stainless-steel chamber, 300 mm in diameter and 1 m long, along the axis of which runs a molybdenum tube  $T$  of diameter 20 mm and a typical length 850 mm, containing samarium metal. The central 400 mm or so of this tube is heated by means of a

cylindrical electrical heater  $H$  with a helical element. Between the molybdenum tube and the heater there is a ceramic tube  $C1$ ; this prevents electrical breakdown, and protects the heater from exposure to samarium if the molybdenum tube should develop a leak. The heater is surrounded by a second ceramic cylinder  $C2$  to provide additional thermal capacity, and outside this there are four cylindrical molybdenum heat shields  $S1$ . Additional molybdenum shields  $S2$  and fiberglass wool insulation  $F$  reduce convective losses at the ends of the heater assembly. The outer oven chamber, including the end plates, is water cooled and enclosed in mu-metal shielding except for the regions allowing access to the laser beam. This reduces the Faraday rotation caused by the Earth's field; there are also coils around the outer chamber, within the mu-metal, which allow accurate cancellation or permit an axial field to be applied for the purpose of recording the Faraday rotation spectrum. For a measurement of rotation produced by samarium vapor the laser beam passes through the central tube; however, the whole oven assembly can be moved sideways, allowing the light to pass through a dummy tube  $D$  outside the heat shields, some 70 mm to one side of the samarium tube and parallel with it. This is important since it allows us to subtract out almost all the rotation which is not due to samarium. However, whether the light travels through the samarium vapor or the dummy tube it must take the same path through all the optical components, since these have enough birefringence due to strain or imperfections to give rotations much larger than those we are studying. The oven chamber is therefore supported on rails attached to the ceiling, while the oven windows  $W$  are attached rigidly to the polarimeter table. They are connected to the oven via rubber tubing  $R$ , which isolates the windows and optical table from vibrations in the oven system, and a system of flexible bellows (e.g.,  $B$ ) where the bellows plates  $P$  are rigidly attached to the rail assembly. The samarium and dummy tubes are open ended, the entire oven assembly being filled with helium buffer gas.

The temperature is monitored using a thermocouple (not shown) placed against the outside of the molybdenum tube in the hot zone. In absolute terms, this gives only an approximate indication of the temperature of the vapor, but it is very useful for monitoring stability. Different transitions required different temperatures; these were found to be broadly consistent with the theoretical  $M1$  transition matrix elements in Table I. The power supply to the oven heater operated under computer control in pulse mode; its output was constant, but the duty cycle could be chosen to give the level of heating

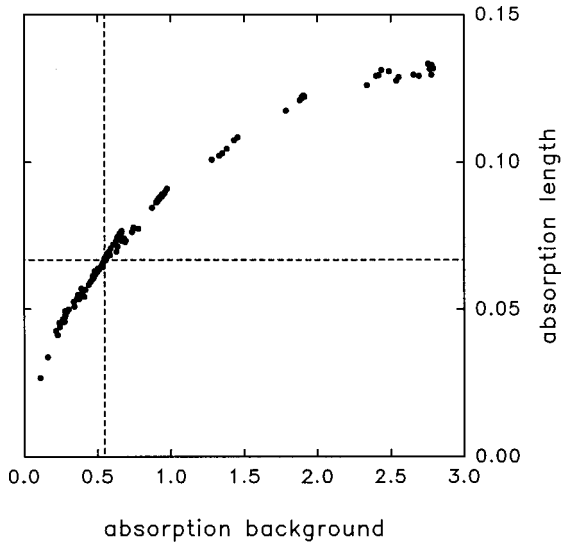


FIG. 4. Relation between the atomic absorption length and the absorption background at 569 nm. Each point represents a different experimental run, where the range of temperatures measured by the thermocouple is approximately 950–1150 K. The abscissa gives the value of the background absorption  $b(\nu)$  and the ordinate the atomic absorption  $pV(\nu)$ , both at line center. These quantities are defined in Eq. (8); both are derived from the absorption fit. For example, the dashed lines intersect at the position of the typical run shown in Fig. 6(c).

required. Angle measurements were made during the intervals between heating pulses.

### C. Choice of experimental conditions

Wolfenden and Baird [14] reported that in their experiments there was evidence of growing contamination of the samarium vapor after oven loading; we therefore cleaned the system thoroughly before loading, and checked carefully that it was leak tight. We found nevertheless that there was considerable background absorption at the positions of all the lines studied. There is evidence that this background was due to samarium itself rather than impurities, and hence unavoidable: for a given oven temperature the fraction  $r$  of the total absorption due to the  $M1$  transition at peak on each of the lines remained closely constant, independent of the length of time since the oven was loaded and from one loading to another. Figure 4 shows the example of 569 nm. Further, the dependence of  $r$  on temperature can be modeled assuming that the background is due to absorption from high-lying levels in atomic samarium. As the temperature increases, both the  $M1$  absorption and the background increase because of the greater vapor pressure. However, the background absorption grows more rapidly because the populations of the high-lying levels increase steeply with temperature. If we make the crude approximation that all these levels are at the same energy  $E'$  above the ground level, the variation of  $r$  with  $T$  shown in Fig. 4 can be fitted quite well using the analysis in the Appendix, giving  $E' \sim 13\,000\text{ cm}^{-1}$ . The implication for the experimental conditions is that for each line there is an optimum  $M1$  absorption length at which to work; too high a value leads to poor signal-to-noise ratio because of the light attenuation due to background absorption.

We did not generally work at this optimum absorption length, preferring instead the lowest at which an adequate signal-to-noise ratio could be achieved. This was in order to maintain stable running conditions for as long as possible; samarium distills out of the hot region of the oven tube, and because (unlike bismuth) it sublimes it does not flow back. This rapidly reduces the number of atoms in the optical path, and leads to blocking of the laser beam by the samarium condensing in the cold region. Typically, a new loading of  $\sim 50\text{ g}$  was required after two days' running.

The highest vapor pressure of samarium at which we worked was about 50 Torr. We used a buffer gas of helium at 50 Torr (as measured at room temperature). Heat loss is primarily due to convection, which is worse in helium than in other rare gases; we carried out some experiments with argon, in which heat losses were considerably reduced. However, helium was chosen for most of the work because it gives the smallest angle noise; convection leads to fluctuations in refractive index, and this effect is far smaller for helium because of its small polarizability in the optical range.

### D. Measurement of angles and absorption

Measurement of intensity, on which our recordings of rotation and absorption spectra are based, is carried out as follows: the detector signal is amplified and sent via a voltage to frequency converter (VFC) to a fast counter in a computer automated measurement and control (CAMAC) system for a period of 1 ms. This is done simultaneously for the three detectors  $D1$ ,  $D2$ , and  $D3$ , as well as those used for the calibration system. To measure the angle of optical rotation, the modulation angles  $\phi_m$ ,  $-\phi_m$ , and 0 produced by the modulator are applied during successive counting periods, giving counts at  $D3$  of  $N_1$ ,  $N_2$ , and  $N_3$ , respectively. To an excellent approximation, we have

$$N_1 = N_0[(\phi + \phi_m)^2 + B], \quad (11)$$

where  $N_0$  is the number of counts which would be recorded under the same conditions if the polarizers were completely uncrossed, and  $\phi$  is any optical rotation additional to  $\phi_m$ . The factor  $B$  ( $\sim 10^{-7}$ ) takes account of imperfections in the optical components which lead to a signal even with the polarizers exactly crossed. Similar expressions can be written for  $N_2$  and  $N_3$ .  $N_0$  depends on the gain of the detection system, but also on the laser intensity and the transmission of the oven, so it changes from point to point on the line profile. The interesting contribution to  $\phi$  is due to samarium, others (including slight uncrossing of the polarizers) being largely eliminated by the double oven system, as explained earlier. To remove laser intensity noise,  $N_1$ ,  $N_2$ , and  $N_3$  are divided by the corresponding signals from the detector  $D2$  to give normalized signals  $S_1$ ,  $S_2$ , and  $S_3$ , respectively. It is necessary to normalize using light which has passed through the oven because some of the laser intensity fluctuations are due to frequency jitter. This translates into intensity jitter if there is frequency-dependent absorption, and the resulting noise at  $D3$  would not be removed if the normalization were carried out using a beam which was not subject to the same effect.

The rotation can then be deduced from these measurements [22]:

$$\phi = \frac{\phi_m}{2} \frac{S_1 - S_2}{S_1 + S_2 - 2S_3}. \quad (12)$$

In practice, a single angle measurement consists of ten successive sequences of six counting periods, in each of which counts are recorded in the order  $N_1, N_2, N_3, N_2, N_1, N_3$  to reduce the effects of drifts. At the conclusion of each sequence, all counts are transferred from the CAMAC system to a computer. The 20 values of each intensity measurement are normalized and averaged before substitution in Eq. (12). These calculations are carried out at the conclusion of each angle measurement, so that spectra together with the calibration fringes can be plotted in real time as a laser scan progresses.

To find the transmission of the samarium vapor, we need measurements of the signals at  $D1$  and  $D3$ . Those at  $D3$  are the  $N_1, N_2$ , and  $N_3$  introduced above; let the corresponding measurements at  $D1$  be  $I_1, I_2$ , and  $I_3$ . We form the quantity

$$g_{\text{Sm}} = \frac{N_1}{I_1} + \frac{N_2}{I_2} - \frac{2N_3}{I_3}, \quad (13)$$

which is proportional to the transmission, and independent of  $B$ . It is put on an absolute scale by dividing by the corresponding quantity  $g_d$  measured at the same laser frequency during a scan on the dummy tube. Because of strong background absorption it was sometimes necessary to use different gains in the  $D3$  detection system on the samarium and dummy tubes, and in these cases the quantities  $g_d$  were scaled appropriately.

### E. Data collection and computer control system

To build up a spectrum, the laser frequency is changed stepwise, data being recorded as described above at 100 frequency points covering a typical range of 10–15 GHz with the transition approximately centrally placed in the scan range. The oven is heated as the laser frequency changes; the exact duty cycle is chosen to give the desired absorption length on the transition being studied, but is typically 50%.

For each line studied, a number of experimental runs were carried out, each giving a value of  $R$  for that transition. A run consisted of several laser scans, typically four with the light passing through the samarium vapor and with a very low net magnetic field (“low-field” scans), one with an applied field of  $\sim 10^{-4}$  T (a “high-field” scan), and four with the light passing through the empty (dummy) tube. The field cancellation for the low-field scans was carried out by periodically adjusting the supply so as to minimize the observable Faraday rotation; this ensured that the level of Faraday rotation was usually no more than typical PNC rotation in heavy elements. Apart from this adjustment, the runs were carried out entirely under computer control. The sequence of low-field and dummy scans, and the direction of the frequency change in a given scan, were chosen so as to minimize the effects of drifts in conditions. At intervals during a series of runs, adjustments were made to the apparatus to change the light path through the system, so that it sampled different areas of the oven windows, the Faraday modulator or the polarizers. This was to randomize as far as possible any re-

sidual PNC-mimicking background rotation not subtracted out by the double-oven system.

The information in the different scans for a given run was combined as follows. The rotation spectra obtained from low field scans were averaged. The same was done with the dummy scans, and the difference array  $\phi_e(i)$  of low-field minus dummy formed, where  $i$  is the channel number in the scan. The high-field rotation spectrum was found by subtracting the averaged dummy spectrum from that obtained in the single scan with the applied field. To obtain the samarium absorption spectrum, first the quantities  $g_{\text{Sm}}(i)$  from different low-field scans were combined by multiplying together the values for a given  $i$ . The same was done for the  $g_d(i)$ , giving two arrays  $t_{\text{Sm}}(i)$  and  $t_d(i)$ ; the transmission of the samarium vapor is then

$$\alpha(i) = \left[ \frac{t_{\text{Sm}}(i)}{t_d(i)} \right]^{1/n}, \quad (14)$$

where  $n$  is the number of scans which have been combined. In fact, the data are put in the form  $\ln \alpha(i)$  for analysis, since from Eq. (8) the  $M1$  contribution to this has a simple Voigt line shape.

Finally, all spectra were put on a linear frequency scale using the calibration provided by the etalon fringes. The output arrays from a run to be analyzed thus consisted of  $\phi_e(\nu)$  and  $\ln \alpha(\nu)$ , and usually also  $\phi_F(\nu)$ . The low-field rotation spectra before subtraction of the dummy, and the averaged dummy rotation spectrum, were used in tests and error diagnostics.

## V. DATA ANALYSIS

### A. General method

To extract experimental values of  $R$  from the runs, theoretical profiles were fitted to the experimental data, using the method of least squares. The value of  $R$  is determined from the analysis of  $\phi_e(\nu)$ . However, we consider first the absorption and Faraday spectra, since they provide information needed for this analysis. Here we describe the general approach; the particular features of each line are dealt with in subsequent sections. Plots are shown of the absorption spectra of all the lines, since the background and its structure varied greatly from case to case. The Faraday and  $\phi_e(\nu)$  rotation spectra are shown for only one line, since the data appear very similar from one to another.

#### 1. Absorption spectrum

The  $M1$  absorption was represented by a Voigt profile, so that the analysis returned values of the Lorentzian and Gaussian widths  $\Delta \nu_L$  and  $\Delta \nu_G$ , the position  $\nu_0$  of the line center, and the optical depth factor  $p$  [Eqs. (6) and (7)]. The analyzed linewidth parameters cannot be interpreted simply in terms of the usual collisional and Doppler broadening mechanisms because they include also the effect of unresolved structure; this is not important, however, so long as the theoretical profile gives an adequate representation of the observed line shape. The analysis was complicated by the presence of frequency-dependent background absorption. The analyzed values of  $\Delta \nu_L$  and  $\Delta \nu_G$  are extremely sensitive to small undulations in the background, and only in favor-

able cases was it possible to float both. Fortunately, floating  $\Delta\nu_G$  with  $\Delta\nu_L$  fixed at a typical value gives a sufficiently accurate representation of the line shape, and this procedure was adopted unless otherwise stated. The background itself was generally represented by a quadratic function of frequency, unless a restricted scan range was being fitted in which case a linear function was sometimes sufficient. Tests of the analysis procedure are described in Sec. V C.

### 2. Faraday rotation

The Faraday rotation is only of interest in that it has to be allowed for adequately in the analysis of the low-field scans  $\phi_e(\nu)$ . This can be done with only one adjustable parameter, an overall scaling factor, provided that the form of the rotation is known. The most satisfactory procedure is to use the rotation spectrum recorded at high field, particularly if there are features in the absorption spectrum which may themselves contribute to the magnetic rotation. However, if it can be established that a theoretical profile derived from the line-shape parameters determined in the absorption fits represents the Faraday rotation spectrum sufficiently well (see Sec. V C), the limited run time of an oven loading can be more efficiently used recording additional low-field data. In practice, we used both methods.

### 3. Rotation spectrum

To analyze  $\phi_e(\nu)$ , we assumed that it consists of  $\phi_{\text{PNC}}(\nu)$ , a Faraday rotation profile, and a residual frequency-dependent background rotation which we represent by a quadratic. There were thus always five parameters to be determined in the analysis, as follows. The Faraday rotation was specified by a single scaling parameter, as explained above. The quadratic introduces three parameters. Finally, the function  $\phi_{\text{PNC}}(\nu)$  is defined by the value of  $R$  [Eqs. (6) and (7)], since the other parameters required,  $\Delta\nu_L$ ,  $\Delta\nu_G$ ,  $\nu_0$ , and  $p$ , were already known. A weighting function was applied in the fitting process, derived from the absorption spectrum, since the signal-to-noise ratio varies significantly over the frequency range recorded.

## B. Features of individual lines

### 1. 662 nm

This line was certainly much the most straightforward to measure and analyze. With a typical  $M1$  absorption length of 1.4, the background absorption was 0.7, giving  $r \sim 0.7$ , the most favorable case studied. The absorption spectrum was well fitted over the whole scan window by a Voigt profile superimposed on a quadratic background; it was possible to float both  $\Delta\nu_L$  and  $\Delta\nu_G$ . Fits to the high-field scans showed that the Faraday rotation could be well represented by Eq. (9), so a theoretical Faraday profile was used in the analysis of the low-field scans. Examples of  $\ln \alpha(\nu)$ ,  $\phi_F(\nu)$ , and  $\phi_e(\nu)$ , with the best-fit theoretical profiles, are shown in Fig. 5.

### 2. 628 nm

The transition strength of this line is almost an order of magnitude less than that of 662 nm. With an  $M1$  absorption length of 0.2, the background was typically 0.4, giving  $r$

$\sim 0.33$ . The background was well represented by a quadratic over the entire scan range in most runs, and it was then possible to float both  $\Delta\nu_L$  and  $\Delta\nu_G$  in the absorption fits [Fig. 6(a)]. However, in some, in which the background was higher because the depletion of the samarium was being offset by working at a higher temperature (see Sec. IV C), it was necessary to restrict the scan range being fitted to a few GHz around the line center. The Faraday rotation was represented by the empirically determined spectrum (the high-field scan) in most cases.

### 3. 611 nm

Although this is the strongest line studied, the Boltzmann factor of the  $J=3$  lower level (0.23 at 1450 K) causes the  $M1$  absorption length to be somewhat lower than the background, i.e.,  $r < 0.5$ . An additional problem was the presence of an initially unidentified absorption feature about 6.5 GHz away toward lower frequency, well within the range in which we would normally carry out a profile analysis, and stronger than the  $M1$  transition itself. The wing of this feature is shown in the absorption plot of Fig. 6(b). The feature was therefore studied to discover whether it was due to some impurity, or to samarium; its origin had to be established if there were to be any confidence in measurements at this wavelength. The authors of Ref. [12] did not observe the feature. A search through the tables of samarium energy levels suggested that a possible candidate was the  $E1$  absorption line  $4f^6 6s 6p \ ^9G_2$  ( $14\,380.50 \text{ cm}^{-1}$ )- $4f^6 6s 7s \ ^7F_3$  ( $30\,755.28 \text{ cm}^{-1}$ ). In fact, a combination of measurements of isotope shifts by saturated absorption spectroscopy and of the relative amplitudes of the Faraday rotation as a function of temperature produced by the feature and the  $M1$  transition confirmed this identification. The field isotope shifts were approximately what would be expected for a  $6s 6p$ - $6s 7s$  transition, while from the Faraday experiments it was possible to deduce that the lower level was at  $\sim 14\,000 \text{ cm}^{-1}$  (see the Appendix). The fact that the lower level of the transition is at such high energy may explain why it was not observed in Ref. [12], whose authors worked at lower temperatures. Also, these authors used higher pressures than ours; the  $M1$  transitions have very small pressure broadening, but the peak absorption of the  $E1$  line would have been considerably reduced by this effect. The change in the relative amplitudes of the Faraday rotation of the  $E1$  and  $M1$  transitions with temperature is quite striking, and is shown in Fig. 7.

The region occupied by the satellite was cut in the absorption fitting. Because of the significant Faraday rotation due to the satellite, the empirically determined Faraday rotation was used exclusively in fitting  $\phi_e(\nu)$ .

### 4. 569 nm

This line had the lowest strength by some margin, and the background was such that it was not feasible to work at an absorption length of more than  $\sim 0.1$ . Even then, the background absorption was a factor of 10 higher [see Fig. 6(c)]. The window over which the absorption spectrum was fitted was restricted to 5 GHz. In most cases the analysis of the rotation spectrum made use of the empirically determined Faraday spectrum.

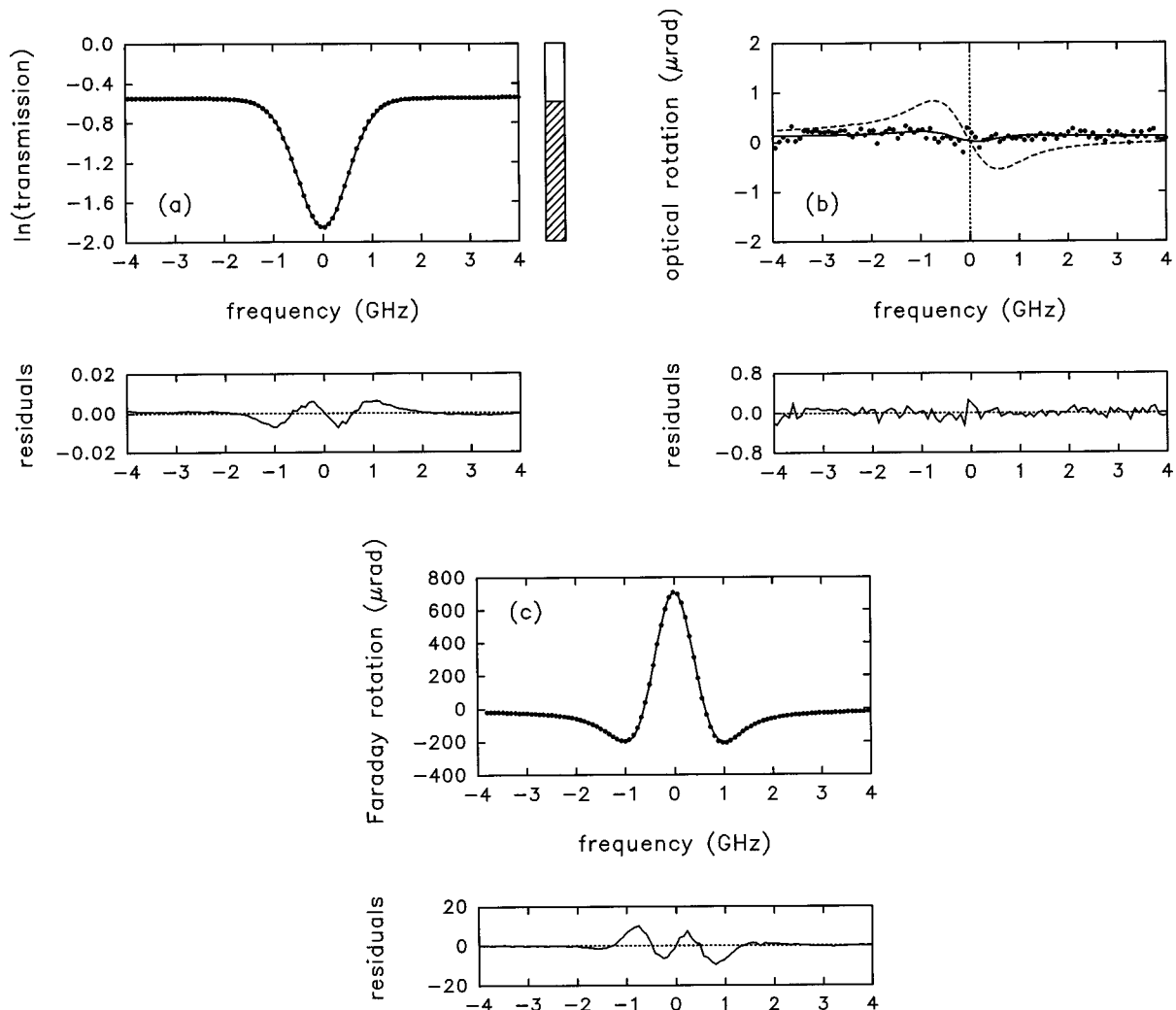


FIG. 5. Fitted spectra for the 662-nm transition: (a) absorption, (b) optical rotation, and (c) Faraday rotation. The absorption and optical rotation spectra belong to the same experimental run. For each spectrum the upper plot shows the experimental data (circles) and the best-fit theoretical profile (continuous line) as a function of frequency detuning from line center; the lower plot shows the residuals (experiment—fit) on the same frequency scale. (a) The indicator to the right of the upper plot shows on a linear scale the fraction  $r$  of the total absorption at line center which can be attributed to the  $M1$  transition, where a fully shaded bar would indicate  $r=1$ , and an empty bar  $r=0$ . The considerable variation of  $r$  from one transition to another can be seen by comparing the corresponding indicators of Fig. 6. Residuals are shown on an expanded vertical scale. (b) The vertical dotted line indicates the line center. The fitted value of  $R$  for this run, using the line-shape parameters from the absorption fit in (a), is  $R=6.4(2.7)$ , in units of  $10^{-8}$ . On the same axes is shown (dashed line) a theoretical profile generated using the same line-shape parameters but with the previous best upper limit on  $R_{662}$  of 100 [14]. Residuals are weighted, and shown on the same vertical scale. (c) Residuals are shown on an expanded scale. Note that experimental Faraday rotation spectra were not taken for parity runs at 662 nm, since as this figure shows the theoretical representation is accurate to a few percent and hence perfectly adequate for modeling the low-field Faraday rotation.

### 5. 558 nm

The lower level of this transition has a Boltzmann factor of  $\sim 0.1$ , so despite its comparative strength the ratio  $r$  is typically only 0.20. There is a weak absorption feature in the blue wing [Fig. 6(d)], which we ascribe to samarium rather than to any impurity, since it was always present at the same level irrespective of the particular oven loading. Its strength relative to that of the 558-nm  $M1$  transition itself increased with temperature, however, suggesting (as with the 611-nm satellite) that it was between two higher-lying levels; in this case, however, the feature was too weak to permit experiments leading to its identification. The region of the feature was therefore excluded from the absorption fits, while any Faraday rotation it produced was automatically taken into

account in fitting  $\phi_e(\nu)$  because the empirical high-field rotation spectra were used to represent  $\phi_F(\nu)$ .

### C. Tests of the analysis procedure

The method of measuring PNC optical rotation applied in the present work evolved over a long program of experiments on bismuth [3,21], during which many tests and checks were carried out to optimize the procedure and minimize the effects of the various error sources. The statistical tests which we apply below to the values of  $R$  given by the various runs, so as to give the best estimate of this quantity and its uncertainty, were developed for bismuth. This earlier work had also established that some potential systematic ef-

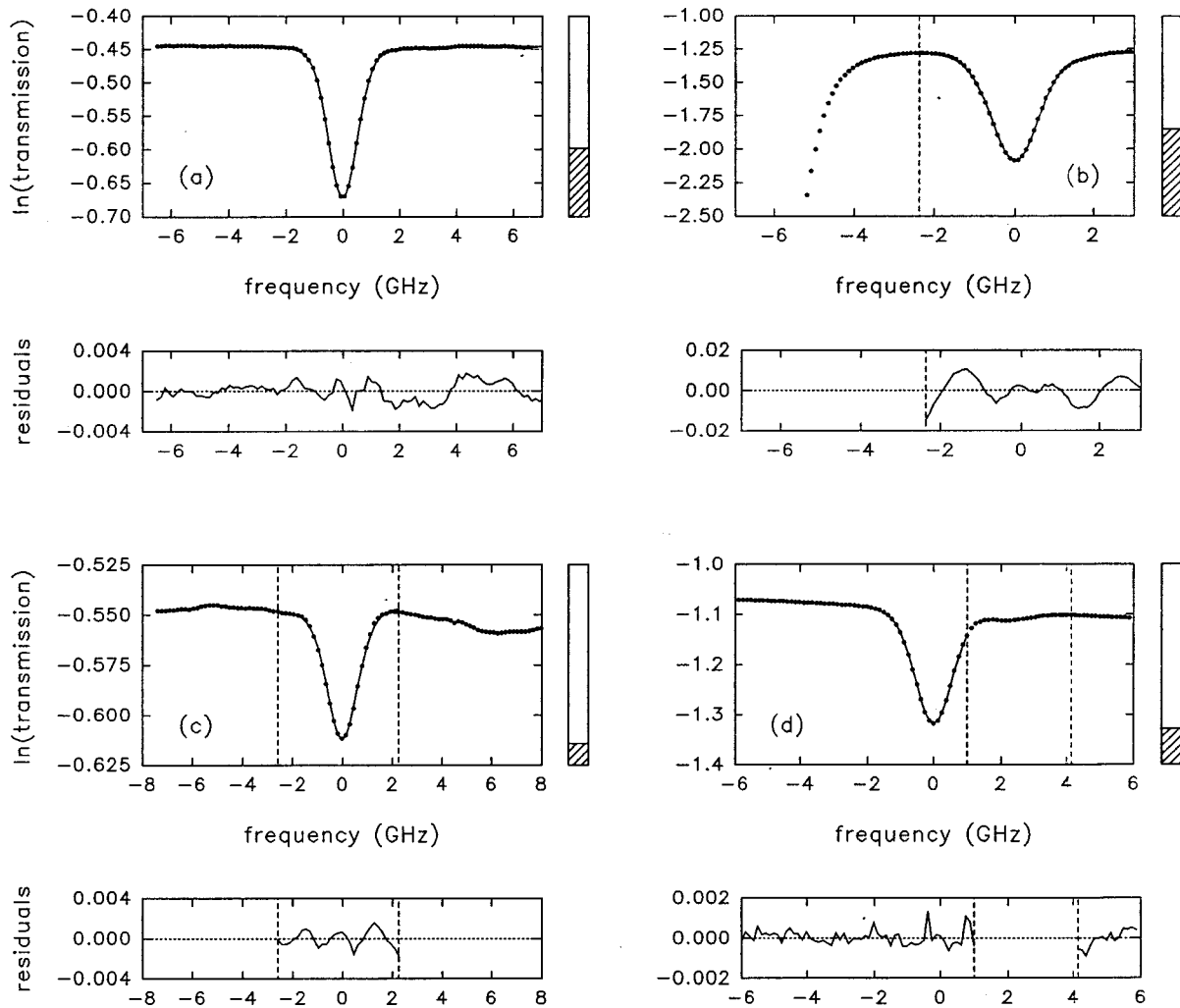


FIG. 6. Fitted absorption spectra for the  $M1$  transitions at (a) 628 nm, (b) 611 nm, (c) 569 nm, and (d) 558 nm. For each spectrum the upper plot shows the experimental spectra (circles) and the best-fit theoretical profile (continuous line) as a function of frequency detuning from line center; the lower plot shows the residuals (experiment-fit) on an expanded vertical scale. The indicator bars to the right of the absorption spectra show the fraction  $r$  of the total absorption at line center which can be attributed to the  $M1$  transition (see the caption to Fig. 5). Fits were carried out over restricted regions in cases (b), (c), and (d), as indicated by the vertical dashed lines, because of features in the background absorption. These are discussed in the text.

facts, such as rotation due to a transverse magnetic field, were negligible at the level of precision of the present experiments. In this section we consider the additional error sources associated with working with samarium.

The major difference between the samarium and bismuth transitions is the number of unknowns in the analysis; bismuth has only one isotope, and the hyperfine structures in the lines studied are accurately known. The samarium  $M1$  transitions all have more than ten components, due to isotopic and hyperfine structure. None of the intervals is known, but the components are close enough together to be completely unresolved. Since we represented this blend by a single component, it was important to establish how much error this could introduce. In particular, the isotopic abundances are greater for the heavier isotopes, leading in principle to an asymmetry in the overall absorption profile.

We constructed simulations of absorption profiles and PNC rotation spectra, assuming that the overall spread of isotopic positions was of the order of the linewidth. We then analyzed them using the single-component approximation

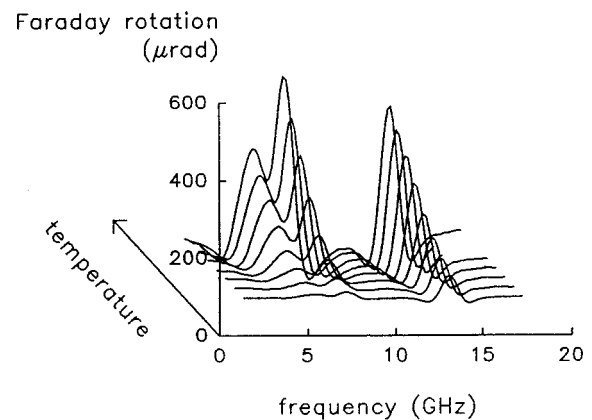


FIG. 7. The variation of the relative line strengths of the satellite line and the  $M1$  transition at 611 nm. The temperatures at which the spectra were taken increase from about 950 to 1100 K in the direction shown. These plots show the Faraday rotation spectra at a constant field, so that (neglecting line-shape variations) the peak rotations are proportional to the numbers of atoms in the lower levels of the transitions.

adopted for the analysis of the genuine data. Even this was an extreme case, since the residuals from a best fit in the simulated absorption spectrum showed systematic behavior significantly worse than those typically encountered in practice. For the purposes of the test the exact relative positions of the individual components are not important, and for simplicity we neglected hyperfine structure and assumed that the isotope shifts were due to the mass effect only. The results showed that the analysed value of  $R$  differed from that used to construct the simulation by less than 1%.

We also established by analyzing high-field scans of the 662-nm line [see Fig. 5(b)] that the Faraday rotation was well represented by Eq. (9), which again makes the single-component approximation. The residuals show systematic trends with frequency only at the level of 1% of the maximum amplitude of the Faraday rotation itself, so that any ‘‘feed-through’’ to the analyzed result for  $R$  in the analysis of the low-field data was negligible. Of course, this still leaves open the possibility that the situation is peculiarly favorable in 662 nm. We therefore also performed analyses of simulations with displaced isotopes, as in the absorption tests, with similar results. The theoretical Faraday profile still neglects any contribution from the background, so when this is appreciable (as in 611 nm) the empirical profile must be used. In the other lines, we do not expect significant rotation except due to the  $M1$  transition itself. The ultimate test of whether we are representing the Faraday rotation adequately in a given line is whether there is a correlation between the analyzed amplitudes of PNC and Faraday rotation (see Sec. V D 2).

Finally, it is necessary to consider any systematic error which might follow from fixing  $\Delta\nu_L$  in the absorption analysis. In fact, tests showed that such an error is negligible; provided this fixed value is also used in fitting  $\phi_e(\nu)$ , together with the value of  $\Delta\nu_G$  obtained from the absorption fit, the analyzed value of  $R$  returned is very insensitive to the exact choice of  $\Delta\nu_L$ .

#### D. Final values of $R$

##### 1. Statistical uncertainty

Scatter plots and histograms are shown for each line in Figs. 8–12. The results with their statistical uncertainties were obtained in the same way for each line, following the general lines of the procedure adopted for the 648-nm line of bismuth [21]. Uncertainties in the Faraday modulator calibration are at the 2% level or below, and can also be safely neglected. For a given line, we first calculate the weighted mean  $R$  using the analyzed values  $R_i$  from the  $n$  individual runs together with the uncertainties  $\Delta R_i$  given by the fitting program. We then calculate the standard error in this mean in two ways: first, using the actual scatter in the data, i.e., from

$$\Delta R = \frac{1}{\sqrt{n}} \frac{\sum_{i=1}^n (R_i - \bar{R})^2 / \Delta R_i^2}{\sum_{i=1}^n 1 / \Delta R_i^2},$$

then purely from the uncertainties  $\Delta R_i$  obtained from the profile analysis:

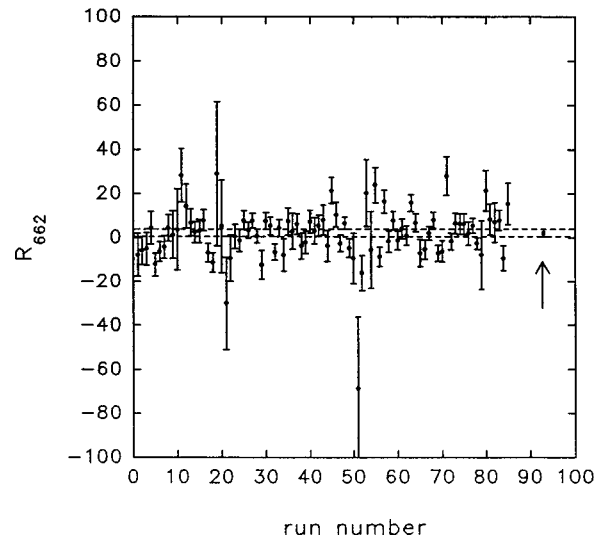
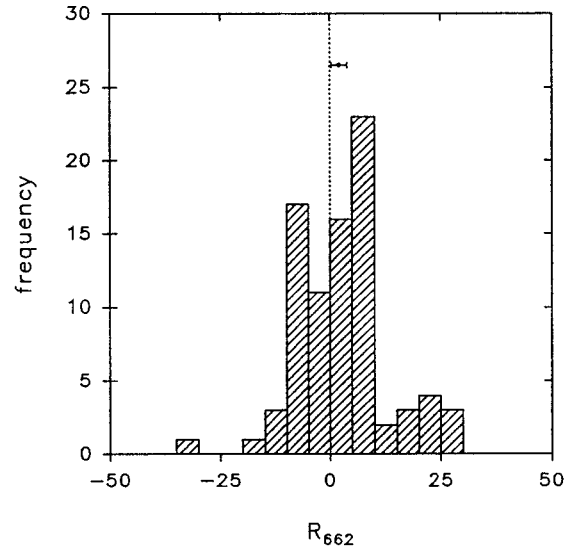


FIG. 8. Histogram and scatter plot for 662-nm analyzed  $R$  values, given in units of  $10^{-8}$ . The final result and error for  $R$  are shown on both figures; on the scatter plot the last point (arrowed) represents the final result, and the dashed lines the error bounds. Error bars on the data in the scatter plot are taken from the uncertainties  $\Delta R_i$  returned by the profile fitting routine before the rescaling procedure described in Sec. V D 1, and are hence underestimated. Note that here, and in Figs. 9–12, one or two outlying data points with very large uncertainties may be omitted from the histogram since its range is smaller than that of the scatter plot.

$$\Delta R_{\text{expt}} = \left[ \sum_{i=1}^n 1 / \Delta R_i^2 \right]^{-1/2}.$$

If the only source of error were statistical variations in the angle measurements across the transition, these two quantities would be closely equal (for values of  $n$  as large as those involved here). However, as Table II shows,  $\Delta R$  is significantly larger. This is because PNC mimicking residual background rotations are always present at some level, and we rely on frequent adjustments to the apparatus to average them out (see Sec. IV E).  $\Delta R_{\text{expt}}$  takes no account of the scatter introduced by this procedure. We therefore add an error  $\delta R$  (the same for the whole data set of a given line) in

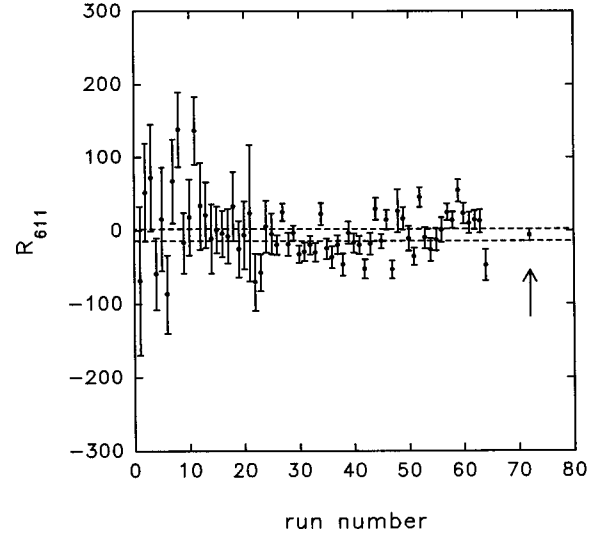
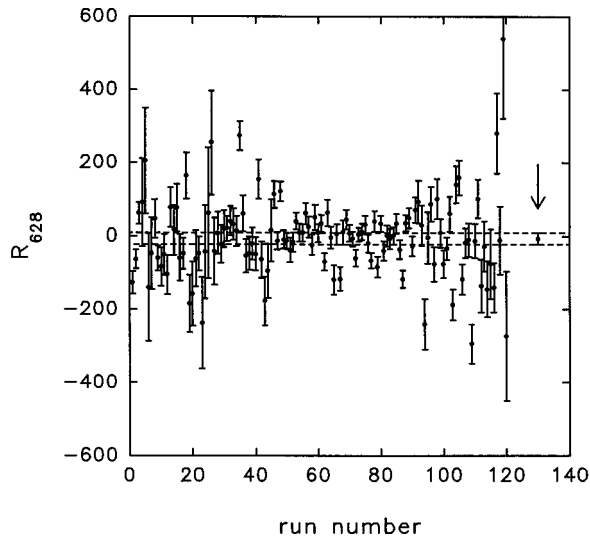
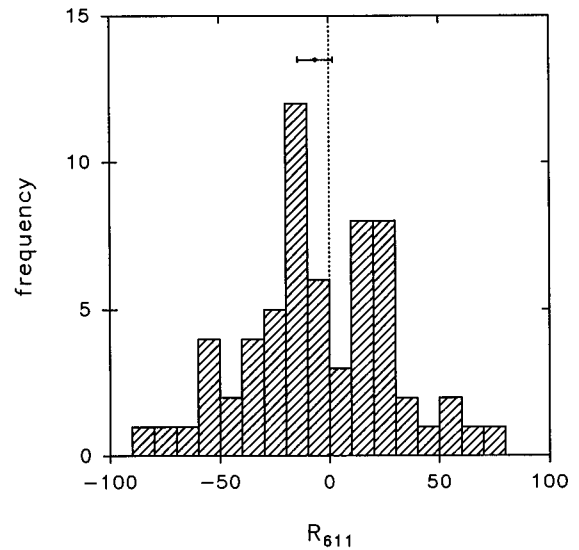
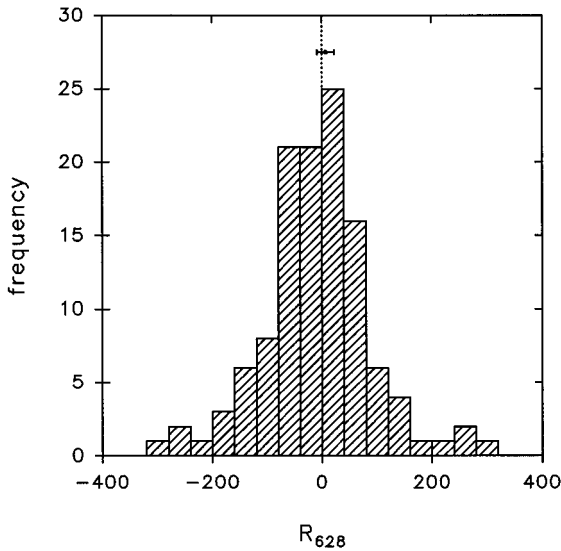


FIG. 9. Histogram and scatter plot for 628-nm analyzed  $R$  values. See the caption to Fig. 8.

FIG. 10. Histogram and scatter plot for 611-nm analyzed  $R$  values. See the caption to Fig. 8.

quadrature to  $\Delta R_i$ , the value being chosen to bring  $\Delta R_{\text{expt}}$  to be equal to  $\Delta R$ . We thus obtain new effective uncertainties  $\Delta R'_i$  in each value of  $R_i$ , from which a new mean  $R'$  and standard error in the mean  $\Delta R'$  are obtained. These quantities are given in Table II.

The next step is to carry out autocorrelation tests on the values of  $R_i$  taken in the order in which they were obtained. If the optical path through the apparatus has not been changed sufficiently often the effective number of independent runs is lower than the number actually recorded, and the uncertainty on the weighted mean must be increased to reflect this. Only one of the lines, 569 nm, required this adjustment, the error being increased by a factor of 1.4.

## 2. Correlation tests

Statistical tests showed no significant correlation between analyzed values of  $R$  and a variety of experimental parameters, including the optical depth and the magnitude of the Faraday rotation. The latter test is an important direct check that the presence of Faraday rotation in the low-field scans

does not lead to systematic error, confirming the conclusions based on simulations and analysis tests described earlier.

## 3. Final results

As in our work on bismuth, the errors on the values of  $R$  as so far derived are minimum estimates, since they only take account of effects demonstrated to be present by the data set itself. To treat the spread produced by our adjustments to the apparatus as statistical is uncertain at the level of the spread itself. We therefore quote as our final results the values obtained as in Sec. V D 1, but with the uncertainties doubled. These are given in Table III. The errors are intended to have the significance of one standard deviation.

## VI. DISCUSSION

The main conclusion from our work is that these lines are certainly not candidates for precise measurement of PNC effects. Even the upper limits on the values of  $R$  are not significantly greater than those found in heavy elements, and the fact that samarium is experimentally unfavorable makes

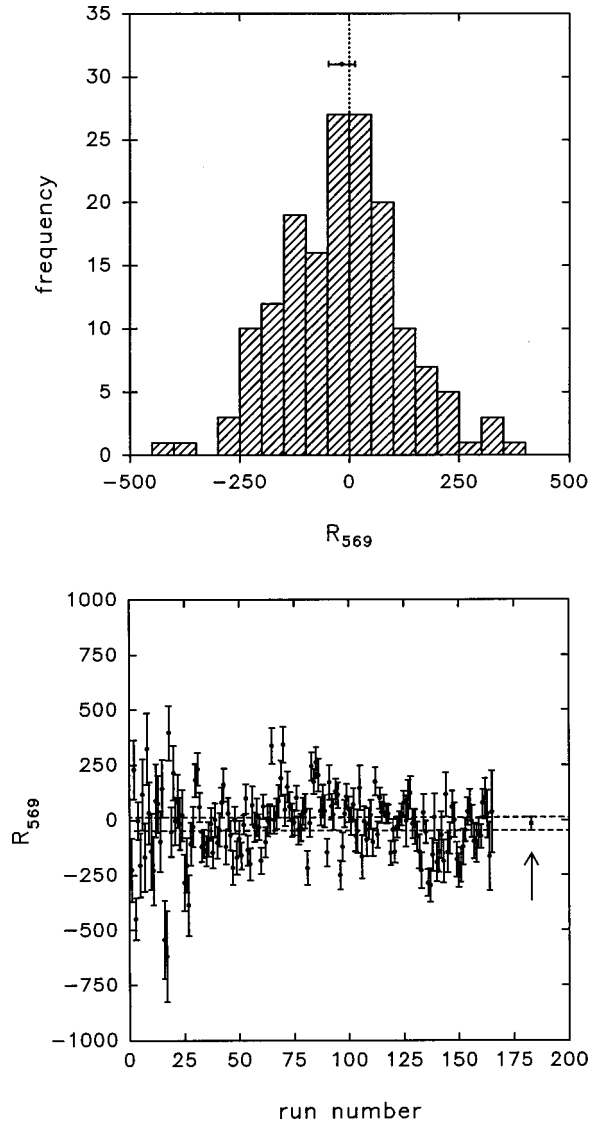


FIG. 11. Histogram and scatter plot for 569-nm analyzed  $R$  values. See the caption to Fig. 8.

matters worse. The transitions thus do not offer the prospect of a critical test of electroweak theory; however, the role of the PNC Hamiltonian in samarium remains interesting as a purely atomic problem. An important point is that since we see no enhancement, we cannot assume that the close-lying levels of opposite parity dominate the PNC admixture in the levels involved in the transitions. We cannot therefore derive unambiguous values for the admixture coefficients from our data; indeed, we cannot even determine their signs, since the PNC rotations are all consistent with zero. However, we can determine the upper limit of the magnitude of the PNC matrix element  $|\langle \alpha J | H_{\text{PNC}} | \beta J \rangle|$ , which would give the maximum rotation consistent with our measurements in each line.

Table IV shows the  $M1$  transitions and the approximate upper limit on  $|R|$  obtained for each. Also tabulated are the corresponding upper limits on the magnitudes of the PNC matrix elements, calculated using Eq. (3). We consider first some features of the individual results, then discuss the wider implications. The  $4f^6 6s^2 \ ^5D_1$  level has two companion levels which could in principle both contribute to PNC mixing; fortunately, our measurements of  $R$  in 662 and 628

TABLE II. Statistical errors in the PNC parameter  $R$  (in units of  $10^{-8}$ ) for the  $M1$  transitions studied. The first three columns after the wavelength  $\lambda$  give the weighted mean  $R$ , the weighted standard error in the mean  $\Delta R$ , and the expected standard error  $\Delta R_{\text{expt}}$ . These quantities are defined in the text. The fourth column gives  $\delta R$ , an extra error added in quadrature to each individual run error to make  $\Delta R$  and  $\Delta R_{\text{expt}}$  equal. The last two columns are calculated using the new run errors to give the weighted mean  $R'$  and the standard error in the mean  $\Delta R'$ .

Wavelength (nm)	$R$	$\Delta R$	$\Delta R_{\text{expt}}$	$\delta R$	$R'$	$\Delta R'$
662	2.0	0.8	0.5	6.2	2.1	0.9
628	-5.1	6.1	3.2	73.3	-7.0	8.0
611	-7.5	3.5	2.1	23.2	-6.1	4.0
569	-11.7	9.6	5.6	111.4	-17.3	10.7
558	-6.6	5.6	3.0	43.6	-6.3	5.8

nm, both of which have  $4f^6 6s^2 \ ^5D_1$  as their upper level, allow separate upper limits to be put on the PNC matrix elements. Our most precise experimental data are for 662 nm, and in addition the measured value of  $R$  is small; this line, therefore, gives a tight constraint linking the two matrix elements  $a = |\langle 4f^6 6s^2 \ ^5D_1 | H_{\text{PNC}} | 4f^6 6s 6p \ ^7G_1 \rangle|$  and  $b = |\langle 4f^6 6s^2 \ ^5D_1 | H_{\text{PNC}} | 4f^6 6s 6p \ ^5D_1 \rangle|$ . The sensitivity to  $b$ , however, is much the greater because the companion transition involved has a larger  $E1$  matrix element. As a result, when we take into account the constraint provided by 628 nm, we obtain a much lower limit on  $b$  than on  $a$ . This limit is particularly disappointing, since the  $LS$  assignments to the two levels involved are the same and one might have hoped for an appreciable admixture.

We obtain critical data from the results for 569 nm, despite the large uncertainty in  $R$ . This is because the  $E1$  matrix element of the companion transition is the largest of the set, and the  $M1$  matrix element the smallest. As a result, the limit set on the PNC matrix element  $c = |\langle 4f^6 6s^2 \ ^5D_2 | H_{\text{PNC}} | 4f^5 5d 6s^2 \ ^7H_2 \rangle|$  by the 569-nm data is better than that given by 611 nm, and at the same level as that on  $b$ , which is derived from our most precise measurements.

We now turn to the reasons why no enhancement is found. The precise optical rotation experiments carried out in lead, thallium, and bismuth have all given values of  $|R| \sim 10^{-7}$ , the same order as the upper limits in Table IV. It is instructive to make a crude comparison between the samarium transitions and the data for one of these elements;

TABLE III. Final values of  $R$  in units of  $10^{-8}$  for the  $M1$  transitions studied in the present work. The errors have a significance of one standard deviation. The results are all consistent with zero.

Wavelength (nm)	$R$
662	2.1(1.8)
628	-7(16)
611	-6(8)
569	-17(30)
558	-6(12)

TABLE IV. Upper bounds on the magnitudes of PNC matrix elements from Eq. (3), using the data in Table I and our measured upper limits on  $|R|$ , given in units of  $10^{-8}$ .

Key: a,  $\langle 4f^6 6s^2 \ ^5D_1 | H_{\text{PNC}} | 4f^6 6s 6p \ ^7G_1 \rangle$ ;  
 b,  $\langle 4f^6 6s^2 \ ^5D_1 | H_{\text{PNC}} | 4f^6 6s 6p \ ^5D_1 \rangle$ ;  
 c,  $\langle 4f^6 6s^2 \ ^5D_2 | H_{\text{PNC}} | 4f^5 5d 6s^2 \ ^7H_2 \rangle$ ;  
 d,  $\langle 4f^6 6s^2 \ ^5D_3 | H_{\text{PNC}} | 4f^6 6s 6p \ ^5F_3 \rangle$ .

Wavelength (nm)	Limit on $ R $	PNC matrix element (kHz)	States
662	3.9	9	a
628	23	1	b
611	14	6	c
569	47	1	c
558	18	30	d

we choose the 876-nm transition ( $6p^3 \ ^4S_{3/2} - 6p^3 \ ^2D_{3/2}$ ) in bismuth, for which  $m = -1.73\mu_B$ . There are refined calculations of PNC effects for this transition [23,24], but these do not allow straightforward extraction of the mixing coefficient.

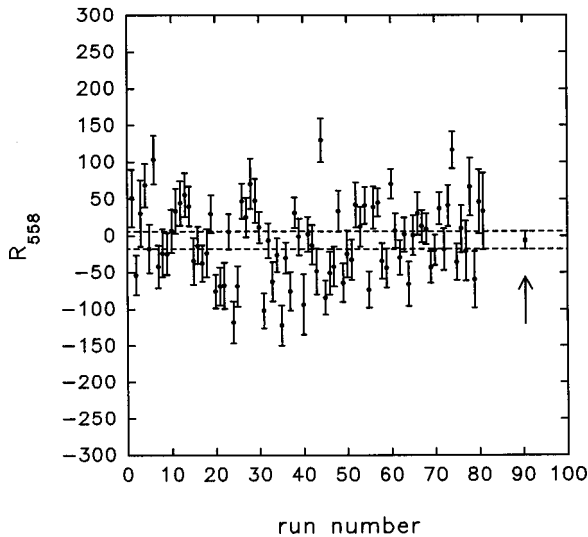
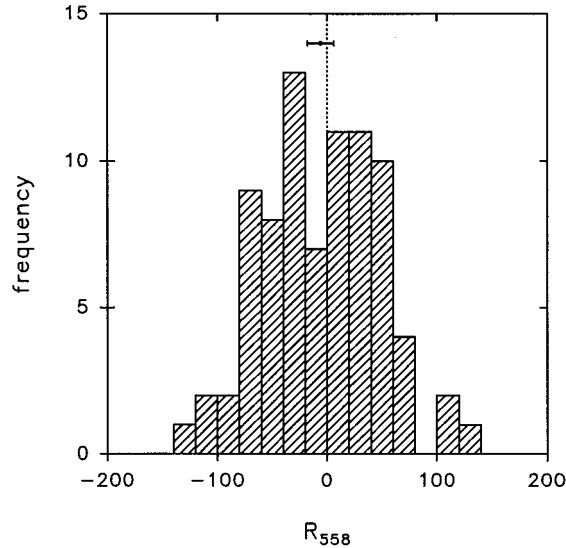


FIG. 12. Histogram and scatter plot for 558-nm analyzed  $R$  values. See the caption to Fig. 8.

For our purposes we consider only the admixture into the bismuth  $6p^3 \ ^2D_{3/2}$  level of  $6p^2 7s \ ^4P_{3/2}$ , some  $33\,450 \text{ cm}^{-1}$  away, since this contributes significantly to the PNC rotation. We can then compare orders of magnitude using Eq. (3). As pointed out earlier, the reason for the initial interest in the samarium transitions is that the energy denominator is so small, being more favorable than that in bismuth by more than two orders of magnitude. It is true that the  $E1$  matrix element for the  $6p^3 \ ^4S_{3/2} - 6p^2 7s \ ^4P_{3/2}$  transition in bismuth is  $\sim 1.4ea_0$  [25], significantly larger than those in Table II. Nevertheless, considering only the energy denominator and the  $E1$  and  $M1$  matrix elements, we could still expect an enhancement of an order of magnitude or more in favour of samarium. The matrix elements of  $H_{\text{PNC}}$  must therefore be substantially smaller in samarium than in bismuth. Substituting the known value of  $R$ , we can estimate crudely the PNC matrix element  $\langle 6p^3 \ ^4D_{3/2} | H_{\text{PNC}} | 6p^2 7s \ ^4P_{3/2} \rangle$  in bismuth using Eq. (3); the result is a few hundred kHz. Since we have considered only one term in the sum, we expect this to be an overestimate, and indeed from the direct calculations of the mixing coefficients [26] we obtain a value of  $\sim 100 \text{ kHz}$ . If the corresponding matrix elements in samarium were as large as this, we would obtain significant enhancement, but, as Table IV shows, they are considerably smaller, some by two orders of magnitude.

We thus conclude that the absence of enhancement is due to two contributory factors: the  $E1$  matrix elements and those of  $H_{\text{PNC}}$  are so low that they offset the potential gain given by the energy denominator. This is disappointing, but understandable, in view of the great complexity of the samarium term diagram. The  $E1$  oscillator strengths are shared among an enormous number of transitions. Also,  $H_{\text{PNC}}$  connects only those components of opposite-parity states which differ solely through the substitution of a  $p_{1/2}$  for an  $s_{1/2}$  electron. The probability that this should be true, or even predominantly so, for the particular pairs of close-lying states of interest in our work is remote, purely on statistical grounds. Further, the very fact that two levels are nearly degenerate implies that there must be more difference between them than the simple promotion of an electron to an excited state.

## ACKNOWLEDGMENTS

This research was supported by the EPSRC. R.B.W. wishes to thank Trinity College, Oxford, for financial support. We are grateful to B. R. Judd for advice about energy levels in samarium, to D. Budker for helpful discussions, and to G. Quelch for expert technical assistance. We thank P. G. H. Sandars for his interest in this work and for a critical reading of the manuscript.

## APPENDIX

Here we show that by measuring the relative absorption lengths or the amplitude of Faraday rotation of two transitions  $X$  and  $Y$  under the same conditions within the same atom one can find the energy  $E_X$  of the lower level of  $X$  given that  $(E_Y)$  of  $Y$ . This is done by carrying out measurements at different temperatures  $T$ , but the temperatures do

not need to be known. This is useful since accurate temperature measurement of a vapor column is difficult.

Let the optical depth factors of the two lines [see Eqs. (7) and (8)] be  $p_X$  and  $p_Y$ . For the present purposes it is sufficient to treat the oven as a uniform vapor column of length  $l$ . Then from Eq. (7) we obtain

$$\ln p_X = \ln N_X + \ln(\kappa_X l), \quad (\text{A1})$$

where  $N_X$  is the number density of atoms in the lower level of transition  $X$ , and  $\kappa_X$  is a constant for that particular transition. To a good approximation,

$$N_X = N_0 \exp(-E_X/k_B T), \quad (\text{A2})$$

where  $N_0$  is the number density of the vapor and  $k_B$  is Boltzmann's constant, so

$$\ln N_X = \ln N_0 - E_X/k_B T. \quad (\text{A3})$$

Over a restricted range, the vapor pressure  $P$  of samarium satisfies [27]

$$\log_{10} P = -A_P/T + B_P, \quad (\text{A4})$$

where  $P$  is in Torr,  $A_P \approx 8300$  K and  $B_P$  is not required in our analysis. Since

$$N_0 = P/k_B T, \quad (\text{A5})$$

we may write

$$\ln N_0 = \ln P - \ln(k_B T), \quad (\text{A6})$$

and, since  $\ln(k_B T)$  is slowly varying,

$$\ln N_0 \approx -A/T + B, \quad (\text{A7})$$

where  $A \approx 19\,000$  K, and  $B$  is a new constant. We thus obtain

$$\ln p_X = \ln(\kappa_X l) + B - (A k_B + E_X)/k_B T, \quad (\text{A8})$$

with a similar expression for  $\ln p_Y$ . Eliminating  $T$ , we find that a plot of  $y = \ln p_X$  against  $x = \ln p_Y$  gives a straight line, with a slope  $m$  given by

$$m = \frac{E_X + A k_B}{E_Y + A k_B}, \quad (\text{A9})$$

from which  $E_Y$  can be determined if  $E_X$  is known.

- 
- [1] M. A. Bouchiat and C. Bouchiat, Rep. Prog. Phys. **60**, 1351 (1997).
- [2] D. N. Stacey, in *Atomic Physics 13*, edited by T. W. Hänsch, H. Walther, and B. Neizert, AIP Conf. Proc. 275 (AIP, New York, 1993).
- [3] M. J. D. Macpherson, K. P. Zetie, R. B. Warrington, D. N. Stacey, and J. P. Hoare, Phys. Rev. Lett. **67**, 2784 (1991).
- [4] D. M. Meekhof, P. Vetter, P. K. Majumder, S. K. Lamoreaux, and E. N. Fortson, Phys. Rev. Lett. **71**, 3442 (1993).
- [5] P. Vetter, D. M. Meekhof, P. K. Majumder, S. K. Lamoreaux, and E. N. Fortson, Phys. Rev. Lett. **74**, 2658 (1995).
- [6] C. S. Wood, S. C. Bennett, D. Cho, B. P. Masterson, J. L. Roberts, C. E. Tanner, and C. E. Wieman, Science **275**, 1759 (1997).
- [7] S. A. Blundell, J. Sapirstein, and W. R. Johnson, Phys. Rev. D **45**, 1602 (1992).
- [8] J. L. Rosner, Phys. Rev. D **53**, 2724 (1996).
- [9] M. A. Bouchiat and C. Bouchiat, J. Phys. (Paris) **35**, 899 (1974).
- [10] V. A. Dzuba, V. V. Flambaum, and I. B. Khriplovich, Z. Phys. D **1**, 243 (1986).
- [11] E. N. Fortson, Y. Pang, and L. Wilets, Phys. Rev. Lett. **65**, 2857 (1990).
- [12] L. M. Barkov, D. A. Melik-Pashayev, and M. S. Zolotarev, Opt. Spektrosk. **66**, 495 (1989) [Opt. Spectrosc. **66**, 288 (1989)].
- [13] D. M. Lucas, D. N. Stacey, C. D. Thompson, and R. B. Warrington, Phys. Scr. **T70**, 145 (1997).
- [14] T. D. Wolfenden and P. E. G. Baird, J. Phys. B **26**, 1379 (1993).
- [15] P. G. H. Sandars, J. Phys. B **23**, L655 (1990).
- [16] A. Carlier, J. Blaise, and M.-G. Schweighofer, J. Phys. (Paris) **29**, 729 (1968).
- [17] *Atomic Energy Levels—The Rare Earth Elements*, edited by W. C. Martin, R. Zalubas and L. Hagan, Natl. Bur. Stand. Ref. Data Ser., Natl. Bur. Stand. (U.S.) Circ. No. 60 (U.S. GPO, Washington, DC, 1978).
- [18] A. Ya. Kraftmakher, Opt. Spektrosk. **66**, 565 (1989) [Opt. Spectrosc. **66**, 968 (1989)].
- [19] A. Gongora and P. G. H. Sandars, J. Phys. B **19**, L291 (1986).
- [20] G. J. Roberts, P. E. G. Baird, M. W. S. M. Brimicombe, P. G. H. Sandars, D. R. Selby, and D. N. Stacey, J. Phys. B **13**, 1389 (1980).
- [21] R. B. Warrington, C. D. Thompson, and D. N. Stacey, Europhys. Lett. **24**, 641 (1993).
- [22] M. J. D. Macpherson, D. N. Stacey, P. E. G. Baird, J. P. Hoare, P. G. H. Sandars, K. M. J. Tregidgo, and Wang Guowen, Europhys. Lett. **4**, 811 (1987).
- [23] V. A. Dzuba, V. V. Flambaum, and O. P. Sushkov, Phys. Lett. A **141**, 147 (1989).
- [24] M. G. Koslov, S. G. Porsev, and V. V. Flambaum, J. Phys. B **29**, 689 (1996).
- [25] *Wavelengths and Transition Probabilities for Atoms and Atomic Ions*, edited by J. Reader, C. H. Corliss, W. L. Wiese, and G. A. Martin, Natl. Bur. Stand. Ref. Data Ser., Natl. Bur. Stand. (U.S.) Circ. No. 68 (U.S. GPO, Washington, DC, 1980).
- [26] V. N. Novikov, O. P. Sushkov, and I. B. Khriplovich, Zh. Eksp. Teor. Fiz. **71**, 1665 (1976) [Sov. Phys. JETP **44**, 872 (1976)].
- [27] *Gmelin Handbuch der Anorganischen Chemie*, edited by G. Kirschstein (Springer-Verlag, Berlin, 1974), Vol. B3.